Applied Surface Science Advances 33 (2026) 100976

Contents lists available at ScienceDirect

Applied Surface Science Advances

journal homepage: www.sciencedirect.com/journal/applied-surface-science-advances

Full Length Article

Corrosion and tribocorrosion behavior of micro-arc oxidized titanium surfaces functionalized with poly(ethylene glycol) and antimicrobial peptides

Natália A. Costa [a,b,c,d], Alexandra C. Alves [d,e], André L. Rossi [f], Ana R. Ribeiro [g], Cláudia Monteiro [b,c], M.Cristina L. Martins [b,c,h,*], Paulo N. Lisboa-Filho [a,*]

[a] UNESP - Universidade Estadual Paulista, Faculdade de Ciências 17033-360 Bauru, SP, Brazil
[b] i3S - Instituto de Investigação e Inovação em Saúde, Universidade do Porto 4200-135 Porto, Portugal
[c] INEB - Instituto de Engenharia Biomédica, Universidade do Porto 4200-135 Porto, Portugal
[d] DEMec - Department of Mechanical Engineering, Faculty of Engineering of University of Porto 4200-465 Porto, Portugal
[e] LAETA/INEGI, Institute of Science and Innovation in Mechanical and Industrial Engineering, R. Dr. Roberto Frias 4200-465 Porto, Portugal
[f] CBPF - Centro Brasileiro de Pesquisas Físicas, 22290-180 Rio de Janeiro, RJ, Brazil
[g] INL - International Iberian Nanotechnology Laboratory, NanoSafety Group 4715-330 Braga, Portugal
[h] ICBAS - Instituto de Ciências Biomédicas Abel Salazar, Universidade do Porto 4050-313 Porto, Portugal

ARTICLE INFO

Keywords:
Titanium
Micro-arc oxidation
Surface functionalization
Poly(ethylene glycol)
Antimicrobial peptides
(tribo)corrosion

ABSTRACT

This paper investigates the corrosion and tribocorrosion behavior of titanium surfaces treated with micro-arc oxidation (MAO) and further functionalized with poly(ethylene glycol) (PEG) and an antimicrobial peptide (AMP). PEG was first covalently conjugated onto the MAO surfaces followed by AMP physical adsorption. The MAO layer maintained its porosity and bulk chemical composition (Ca+*P*) after surface functionalization with PEG-AMP. Although no significant differences on the corrosion mechanisms were observed, the corrosion resistance of the MAO surfaces was slightly improved by the presence of PEG-AMP. This corrosion improvement was mainly attributed to the outer porous oxide layer, where PEG-AMP may create a barrier between the MAO layer and the corrosive medium. In addition, although coefficient of friction (COF) has been slightly increased on the PEG-AMP functionalized MAO surfaces, the bulk titanium was effectively protected under loading and reciprocating sliding conditions, which demonstrates a good tribocorrosion behavior.

1. Introduction

Titanium (Ti) surfaces have been widely studied and tailored by various treatments in the biomedical field, potentially improving their interaction with microorganisms, host fluids and cells. The goal is to address several needs of the bone implant market, such as faster osseointegration, prevention of bacterial infection, and protection against wear and corrosion phenomena [1,2]. The surface functionalization with (bio)molecules represents an emerging and promising strategy. For example, poly(ethylene glycol) (PEG) polymer has been used through different methods to reduce surface bacterial attachment due to its antifouling properties, while immobilized antimicrobial peptides (AMP), as future alternatives to conventional antibiotics, can promote bactericidal activity by altering the bacterial membrane integrity [3–5].

Nevertheless, (bio)molecule-treated Ti surfaces exhibit largely unknown behavior under corrosive and/or mechanical actions. Zhang et al [6] have functionalized AZ31 magnesium alloy surface with a duplex coating: first, it was constructed the bottom layer of MgF_2, followed by a top layer of dopamine cross-linked with polyphenols, serving as anchor points for AMP grafting. The MgF_2 coating remarkably improved the corrosion resistance of the alloy, but its unavoidable minor defects (pores, cracks) may allow the penetration of corrosive compounds to reach the metallic substrate. The presence of organic polyphenolic groups was essential to further enhance the corrosion protection, as released Mg^{2+} from the substrate could be captured into the crosslinked coating through complexation reactions, inhibiting the outflow of Mg ions. The loading of AMP did not alter the induced anti-corrosion properties. Trino et al [7] have deposited a rutile film (500 nm) on Ti substrates, followed by immobilization of osteogenic peptides (dentin

* Corresponding authors.
E-mail addresses: cmartins@i3s.up.pt (M.CristinaL. Martins), paulo.lisboa@unesp.br (P.N. Lisboa-Filho).

https://doi.org/10.1016/j.apsadv.2026.100976
Received 18 November 2025; Received in revised form 6 March 2026; Accepted 13 March 2026
Available online 19 March 2026

matrix protein 1, DMP1) without and with the application of organic spacer molecules, 3-(4-amino- phenyl) propionic acid (APPA) and 3-mercaptopropionic acid (MPA). When peptides were directly attached to the surface (without spacers), the corrosion rate seems to decrease compared with rutile films alone, but higher current density values were observed after the introduction of APPA and MPA. Although the general biofunctionalization has enhanced the corrosion resistance of pristine Ti, the authors pointed out that it is still unclear whether (bio)molecules hind or accelerate electrochemical reactions; in fact, corrosion kinetics may strongly depend on the nature of the organic molecule and the underlying substrate. On the other hand, the good adhesion of peptides onto rutile surfaces seems to provide a stable layer, which may act as a protective and lubricious tribolayer to decrease mass loss during tribocorrosion. However, increased degradation was observed after attaching DMP1 to bare Ti, as the native oxide film was easily damaged, and clusters of negatively charged peptides may have been released from the surface and attracted Ti ions from the metal, consequently boosting their diffusion rate.

Indeed, Ti presents a shortcoming regards its wear resistance, limiting its performance for load-bearing implants. A possible solution is the fabrication of a well-adhered micro-arc oxidation (MAO) layer, acting as a physical barrier against corrosion and wear. Besides Ti, the cost-effective MAO technology (also commonly called plasma electrolytic oxidation, PEO) can successfully develop protective coatings on other metallic materials (magnesium, aluminum, tantalum) of various shapes, demonstrating remarkable adaptability across a wide range of practical domains, including clinical, military, aerospace, and automotive applications [8–12].

MAO Ti layers are typically porous and thick, and can be doped with diverse chemical agents to promote bioactivity or antibacterial performance, including calcium (Ca), phosphorus (P), strontium (Sr), magnesium (Mg), silicon (Si), manganese (Mn), boron (B), zinc (Zn), silver (Ag), and copper (Cu) [13–19]. In addition, at the interface between the bulk metal and the porous coating, a dense oxide film can be grown to impede a possible contact between metal and body fluids that may penetrate into the inner cavities [20,21]. The gradient of crystalline structures along the coating plays also an important role in the wear resistance, combining TiO_2 phases of anatase and rutile, where the latter is more concentrated in the top regions [20,22–24]. As anatase is more ductile and rutile is harder, the resulting MAO Ti coating may present a cushion effect to better accommodate and withstand mechanical stresses [22,25]. However, there is lack of studies to evaluate the degradation (corrosion and/or tribocorrosion) of MAO Ti layers further functionalized with (bio)molecules, including PEG and AMP to combat bacterial infections.

Therefore, this work aimed to investigate the corrosion and tribocorrosion behavior of MAO TiO_2 coatings treated with widely used molecules, namely PEG-based molecules and AMP. First, PEG compounds were covalently conjugated onto the MAO surfaces. Then, the broad-spectrum peptide MSI-78 [26,27] was physically adsorbed onto the PEGylated MAO surfaces. These coatings had previously been examined by our group for their biological performance [28], revealing remarkable antibacterial activity—characterized by low bacterial adhesion and strong bactericidal efficacy against methicillin-resistant *Staphylococcus aureus* (MRSA)—while exhibiting no cytotoxicity toward bone-like cells and effectively supporting osteogenic behavior.

2. Materials and methods

2.1. Processing

2.1.1. Titanium substrate preparation

Grade 4 Ti disks (12.6 mm in diameter; Acnis Brazil) were used as substrates for MAO coating. The nominal chemical composition of grade 4 Ti, as provided by the manufacturer, is specified in maximum weight percentages: 0.50 % Fe, 0.40 % O, 0.08 % C, 0.05 % N, and 0.015 % H, with up to 0.4 % of other elements; balance of Ti. First, the Ti surfaces were subjected to grinding (#150 and #800 mesh SiC papers) and ultrasonically cleaned in propanol-filled bath for 10 min. Then, the specimens were etched by Kroll's solution ($HF:HNO_3:H_2O = 1:1:1$ in volume; acidic reagents from Honeywell, Fluka) to remove any remaining contaminants and facilitate the formation of a fresh oxide film. Afterwards, the specimens were washed in an ultrasonic bath of propanol (10 min) and Type II water (5 min) (Type II water: distilled water, resistivity > 1 MΩ.cm, a conductivity < 1 μS/cm and < 50 ppb of total organic carbons), and dried at room temperature (RT).

2.1.2. Micro-arc oxidation

Based on previous works [20,29], the MAO treatment was conducted using a direct current (DC) power supply (Keysight Technologies N5751A), with a limiting current of 2.5 A and under a voltage of 300 V. The exposed areas of the anode (specimen: grade 4 Ti substrate) and the cathode (grade 2 Ti plate, Sandinox) were 0.94 cm^2 and 1.70 cm^2, respectively. The distance between electrodes was set as approximately 7 cm. The electrolyte was selected to incorporate calcium and phosphorus into the coatings, through the composition of 0.35 M calcium acetate monohydrate and 0.02 M β-glycerophosphate disodium salt pentahydrate (Sigma-Aldrich) in Type II water. Surfaces were treated for 1 min under magnetic agitation (500 rpm) and at RT. Ultimately, the specimens were rinsed with Type II water and propanol, and dried with air stream at RT. The MAO-treated specimens were called MAO-control.

2.1.3. Surface (bio)molecule immobilization

MAO specimens were dried in a vacuum oven (20–40 mbar, 100 °C, 24 h) to minimize physical adsorption of water. Subsequentially, the coatings were activated by O_2 plasma, using a non-destructive protocol to create surface hydroxyl groups, according to [20]. The following parameters were employed in the plasma cleaner equipment (Tergeo, Pie Scientific, TG100): radio frequency (RF) source at 75 W, pulse of 255 (N/255), O_2 flow rate of 50 sccm, plasma direct mode for 2 min, and 1.3 mbar chamber pressure.

After plasma activation, the specimens were immediately transferred to a glove chamber saturated with dried N_2, in order to perform the molecule immobilization procedure. Specimens were immersed in a solution containing the following compounds/concentrations: (i) a carboxyl-PEG_{113}-maleimide molecule (HOOC-PEG-MAL; JenKem Technology Co.; 1 mg/mL), (ii) a coupling agent 1-(3-dimethylaminopropyl)-3-ethylcarbodiimide hydrochloride (EDC; Thermo Scientific; 10 mg/mL), and (iii) a catalyst 4-(dimethylamino)pyridine (DMAP; Sigma-Aldrich; 2 mg/mL). The carboxyl motif from the PEG molecule was linked with the surface hydroxyl species from activated MAO coatings, using EDC and DMAP to induce covalent grafting. The reagents (i, ii, and iii) were dissolved in dry dichloromethane as solvent. The reaction between the PEG molecules and MAO coating (to fabricate PEGylated MAO surfaces) was carried out overnight, 100 rpm, RT, and protected from light. After that, the specimens were washed twice with tetrahydrofuran (THF; Thermo Scientific), and three times with Type II water to be subsequentially incubated in peptide solution.

The AMP solution was prepared with MSI-78 (GenScript Biotech Corporation; sequence of amino acids: GIGKFLKKAKKFGKAFVKILKK) at 0.5 mg/mL in phosphate buffer at pH 6.6. The immobilization process of peptide MSI-78 onto the PEGylated MAO surfaces took place for 24 h, 100 rpm, RT, protected from light. After AMP treatment, specimens were ultrasonically cleaned in Type II water for three times during 2 min, followed by immersion in 70 % v/v ethanol (2x for 15 min) and three-time rinsing in Type II water. Then, the (bio)molecule-containing MAO coatings were dried with a gentle stream of argon. For nomenclature, PEGylated MAO surfaces treated with AMP were referred to as MAO-PEG-AMP. The same protocol was employed to prepare PEGylated MAO surfaces, but only incubated in phosphate buffer (without peptide), in order to evaluate the PEG effect alone; these specimens were named as MAO-PEG. Fig. 1a shows the surface (bio)molecule

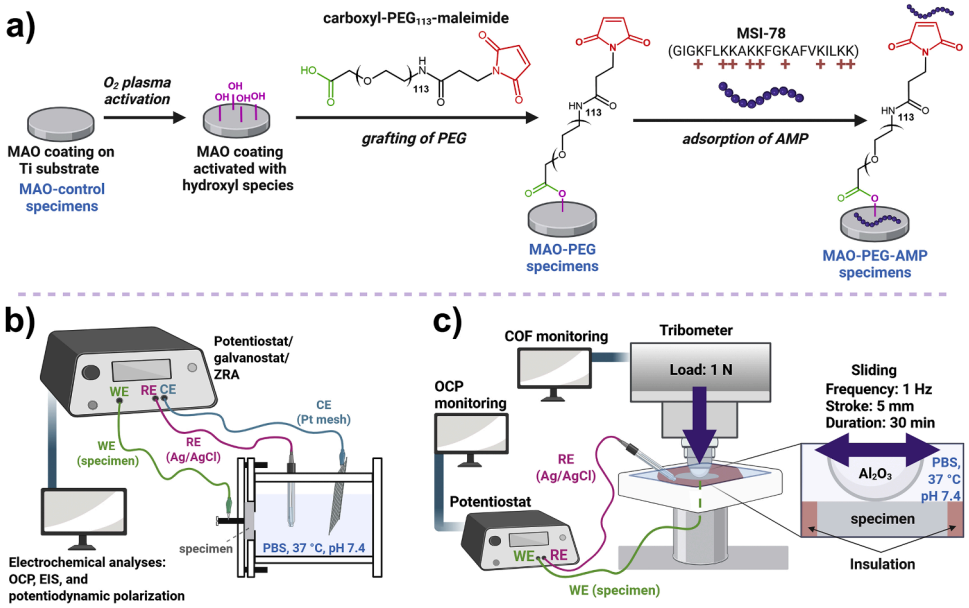

Fig. 1. (a) Schematic representation of the (bio)molecule immobilization (PEG and AMP) onto MAO surfaces (not to scale). Set-up for (b) corrosion and (c) tribocorrosion tests.

immobilization schematically.

2.2. Corrosion tests

Electrochemical analyses including open circuit potential (OCP) monitoring, electrochemical impedance spectroscopy (EIS), and potentiodynamic polarization tests were performed sequentially, using a three-electrode set-up (adapted from ASTM: G3–89 standards, Fig. 1b) in 200 mL phosphate-buffered saline (PBS) electrolyte (GRiSP Research Solutions) at physiological temperature of 37 °C and pH 7.4. The electrochemical cell was placed in a climate chamber to maintain the temperature, and the chamber also acted as a Faraday cage to avoid any external currents. Specimens served as working electrode (WE) with an exposed area of 0.38 cm^2, a mesh of platinum (Pt) was used as counter electrode (CE), and the reference electrode (RE) was a saturated Ag/AgCl electrode. All the measurements were recorded through a Gamry Instruments Potentiostat/Galvanostat/ZRA (model Reference 600+).

OCP values were continuously monitored for at least 3 h to ensure system stabilization. Such stability was considered when OCP did not present a variation higher than 60 mV within the last hour of immersion. Sequentially, EIS spectra were acquired at OCP, ranging frequencies from 10^5 till 10^{-2} Hz, with 7 points per frequency decade, and a sinusoidal signal with an amplitude of 10 mV. Afterwards, potentiodynamic polarization tests were conducted from −0.25 V_{OCP} to 1.50 $V_{Ag/AgCl}$ using a scanning rate of 0.50 mV/s. All electrochemical measurements were conducted at least on three independent specimens, and the average values were reported with the corresponding standard deviation.

2.3. Tribocorrosion tests

Tribocorrosion experiments were performed using a tribometer (CETR-UMT-2) with a reciprocating ball-on-disk configuration (Fig. 1c). Specimens were mounted in the tribo-electrochemical cell that was filled by PBS (pH 7.4) as electrolyte, at 37 ± 2 °C. A two-electrode set-up was connected to a Gamry Instruments Potentiostat/Galvanostat/ZRA (model Reference 600+), wherein a saturated Ag/AgCl electrode served as RE, and the specimens were established as WE. OCP was measured before, during, and after sliding. Prior to sliding, the OCP was measured till stabilization and it was considered stable when a variation in potential was below 60 mV/h. During mechanical solicitations, the coefficient of friction (COF) values was also registered using a UMT-2 software coupled to the tribometer. The counter-body was an alumina (Al_2O_3) ball with 10 mm of diameter (Ceratec), to slide for 30 min on the specimens' surface, with a total stroke length of 5 mm, at a frequency of 1 Hz, and applying a 1 N normal load (corresponding to a maximum Hertzian contact pressure of 410 MPa for untreated Ti). After tribocorrosion tests, specimens were rinsed with Type II water and dried with air stream at RT. At least three replicates were assessed to ensure repeatability of the results.

2.4. Ion release studies

The specimens were immersed individually in 40 mL PBS for 7 days at 37 °C. Ion concentrations (Ti, Ca and P) present in the solution were measured at different immersion time-points of 5 h, 1 day, 2 days, 4 days, and 7 days. At each time-point, 8 mL of the solution immersed with the specimen were collected to be evaluated, and three independent assays were carried out. PBS was also analyzed as background.

The concentration of P was determined by UV/Vis spectrophotometry (UV/Vis Thermo Spectronic Genesys 6), through the vanadomolybdophosphoric acid method. For calibration, standard solutions of phosphorus were prepared from the dilution of 1.25 mmol/L monopotassium phosphate (KH_2PO_4), and with the addition of nitric-vanadomolybdate (chromogenic reagent). Those solutions were measured in terms of absorbance signals, using absorption wavelength of 420 nm. The chromogenic reagent was set as blank. The optimal range of concentration of the analytical curve was 1–10 mg/L. The equation for the calibration plot was as follows: $Abs = 0.03705 \times C_P + 0.02695$, $r = 0.9998$.

The concentration of Ca was obtained via flame atomic absorption spectroscopy (FAAS), while Ti was analyzed via graphite furnace atomic absorption spectrometry (GFAAS) (Shimadzu AA-6800 spectrometer). Self-reversal background absorption correction was employed. A Shimadzu hollow cathode calcium or titanium lamp was operated at a minimum current of 12 mA.

For the determination of Ca, the following operational conditions were applied: λ = 422.7 nm, spectral resolution: 0.5 nm, flame stoichiometry: oxidizer, flame type: air-acetylene, and gas flow: 2 L/min.

To determine Ti, the following parameters were used: λ = 364.3 nm,

spectral resolution: 0.5 nm, and inert gas: argon. The gas flow was maintained at 1 L/min throughout the heating program, and it was stopped for the atomization stage. The heating program of the graphite tube presented the respective temperatures, according to [30]: drying - 120/250 °C; pyrolysis - 900/1400 °C; atomization - 2600 °C, and cleanup - 2800 °C.

Blank solutions were prepared by a mixture of 0.010 mol/L NaH_2PO_4 and 0.1370 mol/L NaCl (for Ti determination), with the addition of 10 g/L of lanthanum (for Ca determination). Then, analytical curves were constructed from the dilution of Titrisol standards (Merck) of the analytes. The absorbance measurements were based on the peak area. The equations for the calibration curves were as follows: Ca: Abs = 0.0544 x C_{Ca} - 0.01650, r = 0.9992; Ti: Abs = 0.02608 x C_{Ti} - 1.5 × 10^{-5}, r = 0.9999.

2.5. Characterization of the coatings

Morphology and chemical composition of the specimens were evaluated by scanning electron microscopy (SEM; Phenom XL G2, Thermo Scientific) and energy dispersive X-ray spectroscopy (EDS; software integrated in Phenom user interface). Detectors for secondary electron and backscattered electron (BSE) were used, within 10–15 kV accelerating voltage. The results of chemical composition given by EDS analysis (n = 3) are presented as average ± standard deviation.

Top surface chemical composition was acquired by X-ray photoelectron spectroscopy (XPS; ESCALAB 250Xi, Thermo Fisher Scientific), operating a monochromatic Al Kα X-ray source (1486.68 eV) at 220 W. Survey (wide) scans were recorded using pass energy of 100 eV and energy step size of 1.0 eV. High-resolution spectra were collected using pass energy of 40 eV and energy step size of 0.1 eV. High-resolution regions were fitted and calculated by the CasaXPS data processing software, employing the Shirley-type background and relative sensitivity factors provided by the library. C 1 s (284.6 eV) was used as calibration energy.

Cross-section of the coatings was investigated by transmission electron microscopy (TEM). For that, a lamella was prepared by a focused ion beam (FIB; Tescan Lyra 3 dual beam), with a gallium ion source. Platinum layers were deposited using 0.2 nA ion current and beam energy of 30 keV. Slices and bulk milling were performed through ion currents varying between 1 and 5 nA, accelerated at 30 keV. Fine milling (polishing) was conducted by using 0.1 nA/10 keV and 10 pA/5 keV, to obtain a lamella with approximately 100 nm of thickness. TEM analysis was carried out at an accelerating voltage of 200 kV (JEOL 2100F).

Crystal structure of the coatings was evaluated by X-ray diffraction (XRD; X'Pert PRO, PANanalytical), with Ni-filtered CuKα radiation and a PIXcel detector, operating at 45 kV and 40 mA, scan between 20° and 60° (2θ) (Bragg-Brentano geometry), step size of 0.02°. Phase identification was performed by comparing with standard reflections from Inorganic Crystal Structure Database (ICSD) (card numbers: anatase #9852, rutile #33837, and titanium #253841). The phase percentage was calculated through the following Eq. (1):

$$\%phase_{\alpha} = \frac{\sum I_{\alpha\ peaks}}{\sum I_{all\ peaks}}\ x\ 100 \quad (1)$$

3. Results and discussion

3.1. Synthesis and characterization of the coatings

The surface morphology of the coatings is presented in Fig.2a–c. The introduction of PEG or PEG-AMP did not alter the microstructure, with an extensive surface porous network due to the formation of micro-arcs during anodic treatment [23,29]. The elemental EDS mappings of the MAO-control specimens are shown in Fig. 2d. The high temperatures of the micro-arcs can promote the localized melting of the oxide, allowing its doping with bioactive elements from the electrolyte, such as Ca and P. No significant changes in EDS mapping were observed for MAO-PEG and MAO-PEG-AMP specimens (Fig. S1 in Supplementary Material). Semi-quantitative chemical analysis by EDS is given in Fig. 2e. Similar content of Ca and P was noticed between the groups, indicating that the procedures for (bio)molecule immobilization did not modify the bulk chemical composition of the MAO layer. The atomic Ca/P ratios of 3.45 ± 0.27, 3.53 ± 0.29, and 3.53 ± 0.24 were found for MAO-control, MAO-PEG, and MAO-PEG-AMP specimens, respectively.

As the EDS method is not sensitive to light elements, the XPS technique was applied to detect nitrogen and verify the surface immobilization of PEG and AMP (Fig. 3). All the coatings presented Ca and P at the surface (Fig. 3a), and there is the introduction of N 1 s signal after treatment with molecules (Fig.3a,b), indicating the successful surface immobilization of PEG and AMP. From the high-resolution XPS spectra, the N/Ti ratios of 0.11 and 0.96 were found for MAO-PEG and MAO-PEG-AMP coatings, respectively.

The cross-section of the MAO-control coating is presented in Fig. 4. As surface morphology (SEM) and bulk chemical composition (EDS) were maintained after molecule immobilization, cross-sectional analyses were not performed for MAO-PEG and MAO-PEG-AMP specimens.

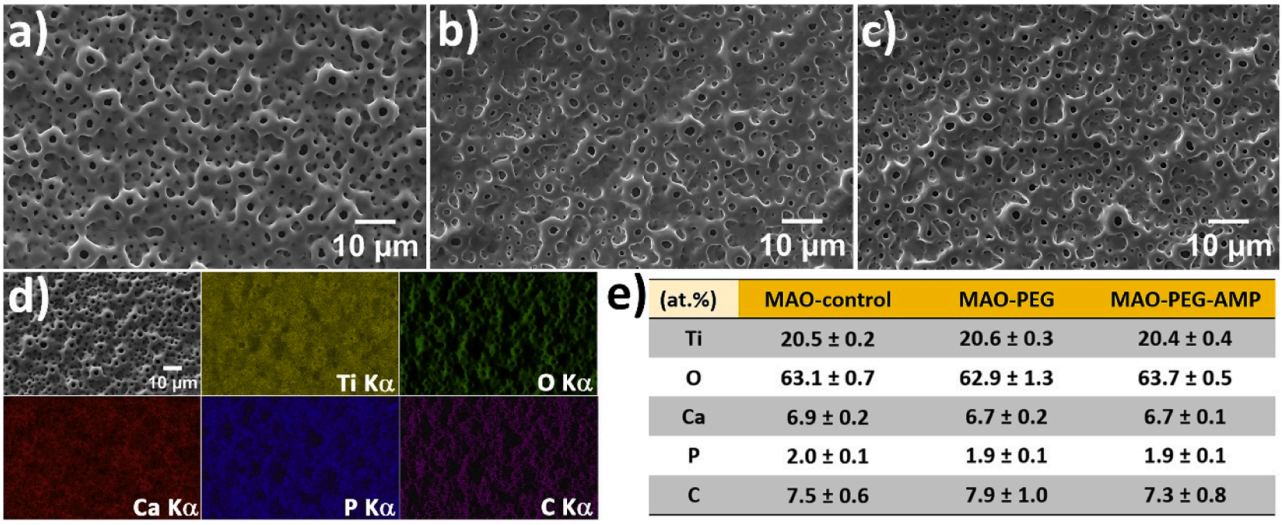

(at.%)	MAO-control	MAO-PEG	MAO-PEG-AMP
Ti	20.5 ± 0.2	20.6 ± 0.3	20.4 ± 0.4
O	63.1 ± 0.7	62.9 ± 1.3	63.7 ± 0.5
Ca	6.9 ± 0.2	6.7 ± 0.2	6.7 ± 0.1
P	2.0 ± 0.1	1.9 ± 0.1	1.9 ± 0.1
C	7.5 ± 0.6	7.9 ± 1.0	7.3 ± 0.8

Fig. 2. Surface morphology of (a) MAO-control, (b) MAO-PEG, and (c) MAO-PEG-AMP specimens, obtained by SEM. (d) Elemental EDS mappings of the MAO-control specimens. (e) Atomic concentration given by semi-quantitative EDS analysis.

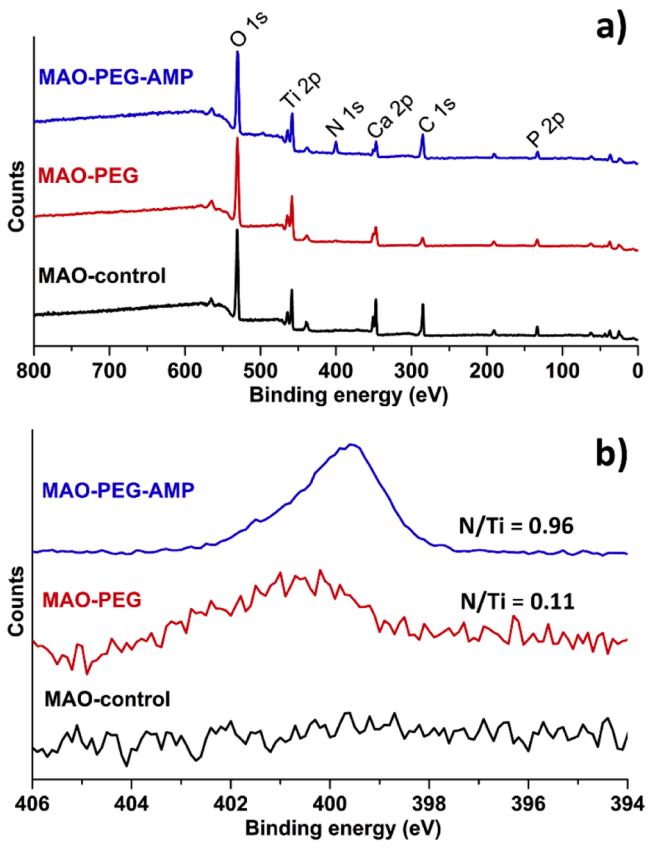

Fig. 3. XPS analysis of the coatings. (a) Survey spectra and (b) high-resolution N 1 s spectra, together with calculated N/Ti ratios.

The anodic coating presented three different layers. Adjacent to the titanium substrate, there is the formation of a compact film (A), related to the stage of oxide growth by conventional anodization. The following layer (B) is characterized by small pores, which could be originated by micro-arcs due to the dielectric breakdown of the oxide, as well as bursts of oxygen-filled cavities due to local high pressures [23]. The outer porous layer (C) presented bigger pores, likely due to more potent micro-arcs during the later periods of the treatment.

The phase composition (XRD) of the MAO-control coating is presented in Fig. 5. The extremely high temperatures provoked by the micro-arcs have resulted in a TiO_2 layer composed of crystal phases of anatase (79 %) and rutile (21 %), with R/A ratio of approximately 0.27. Similar crystalline proportion was identified in previous work [23] using the same MAO electrical parameters, but with a different Ti-based substrate (Ti-40Nb alloy).

The ion release profiles from the coatings in PBS are presented in Fig. 6. In general, a higher quantity of phosphorus (Fig. 6a) was released from the coatings as compared to the levels of calcium (Fig. 6b). Titanium release was also studied, and this element was only detected after 4 days of immersion, with significantly low values (< 0.01 mg/L) for all the coatings (data presented in Table S1, Supplementary Material). In terms of phosphorus (Fig. 6a), its dissolution was decreased after the treatment with (bio)molecules, especially when PEG was combined with AMP (MAO-PEG-AMP coatings). On the other side, MAO and MAO-PEG coatings presented a similar release profile of calcium (Fig. 6b), and the surface introduction of AMP slightly increased this calcium release. These results indicate that (bio)molecules immobilized onto MAO coatings may alter their ion release behavior, which seems both dependent on the chemical element to be released, and type/surface conformation of immobilized molecule.

3.2. Corrosion behavior

The OCP evolution for the last 10 min of immersion and representative potentiodynamic polarization curves are presented in Fig. 7. In addition, the average values for open circuit potential (E_{OCP}), corrosion potential ($E_{(i\,=\,0)}$) and passivation current density (i_{pass}) extracted from potentiodynamic polarization curves are given in Table 1. Similar

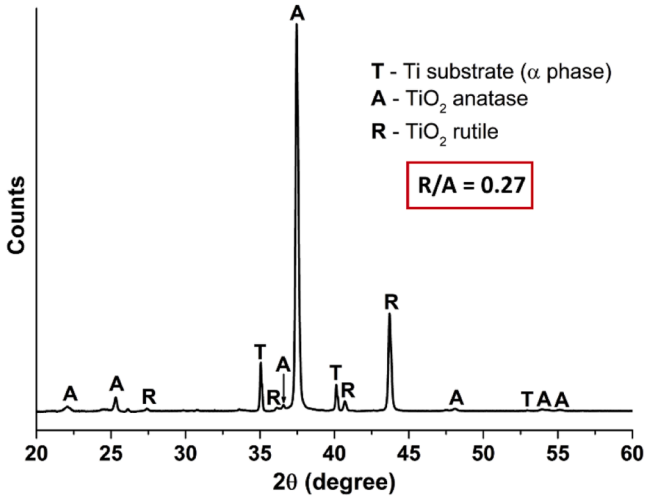

Fig. 5. XRD pattern of the MAO-control coating.

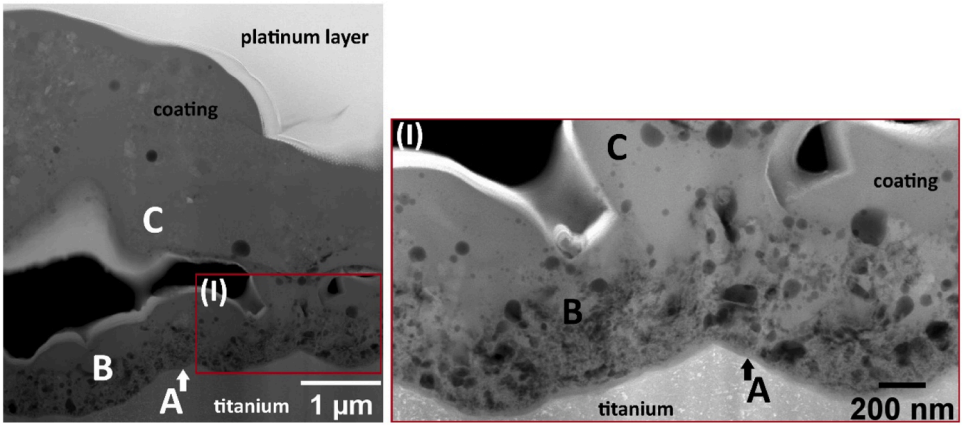

Fig. 4. FIB-prepared cross-section of the MAO-control coating. The morphology was analyzed by dark field-STEM images, with higher magnification selected zone (in red box, I). The coating presented three different layers (A, B and C).

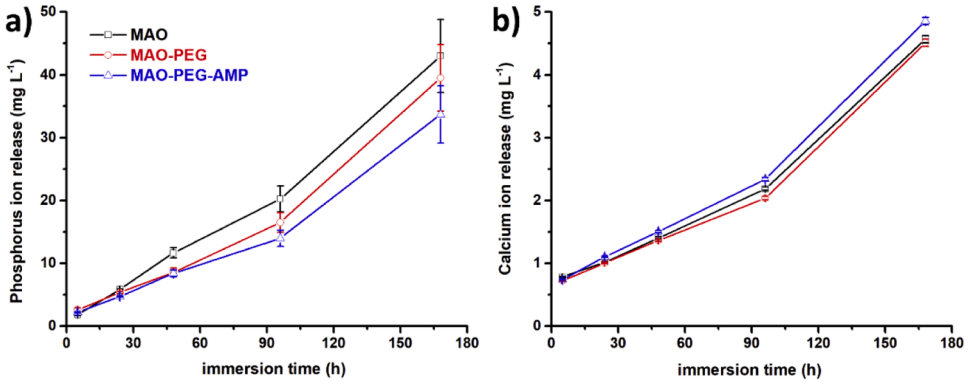

Fig. 6. Ion release profiles of (a) phosphorus and (b) calcium from the coatings in PBS over 7 days.

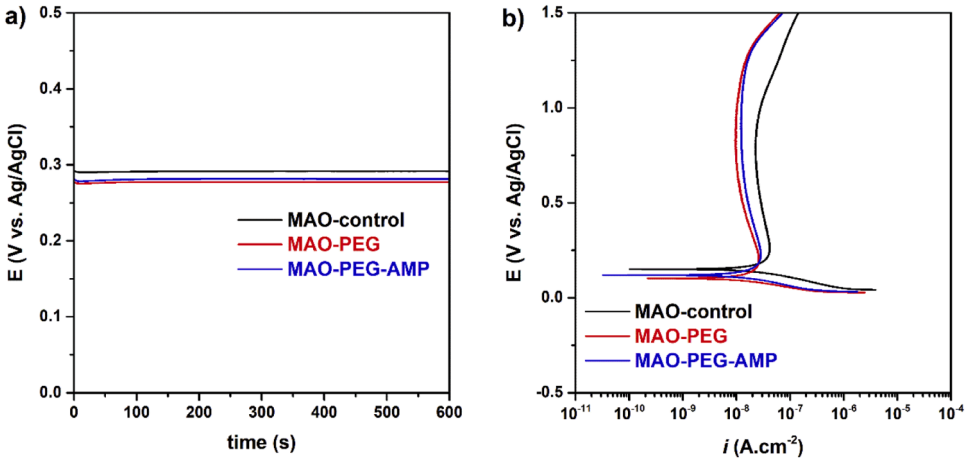

Fig. 7. (a) Representative OCP evolution during the last 10 min of immersion in PBS at body temperature and (b) representative potentiodynamic polarization curves for MAO-control, MAO-PEG and MAO-PEG-AMP coatings.

corrosion susceptibility was exhibited for MAO-control and MAO-PEG coatings (E_{OCP} values of 0.29 ± 0.00 and 0.28 ± 0.01 $V_{Ag/AgCl}$, respectively), while MAO-PEG-AMP presented slightly lower but still positive average OCP values (0.19 ± 0.12 $V_{Ag/AgCl}$).

Regarding the $E_{(i\ =\ 0)}$, MAO-PEG-AMP specimens presented the lowest average values, 0.08 ± 0.07 $V_{Ag/AgCl}$. On the other hand, the average i_{pass} values showed a slight decrease after functionalization with the (bio)molecules, mainly for MAO-PEG coatings. All coatings of this work exhibited significantly lower i_{pass} values (2-log reduction) compared to bulk Ti or Ti-based alloys in PBS [31,32], thereby confirming the corrosion-protective nature of the coatings. Other previous studies consistently demonstrate that MAO treatment can improve the corrosion resistance of Ti-based materials; however, differences in electrolyte composition—such as the use of simulated body fluid (SBF) to reproduce physiological conditions [33–35] or 3.5 % NaCl solution to replicate marine environments [36]—may influence the extent of improvement observed. When 0.9 % NaCl solution was employed as the corrosive medium, earlier research reported i_{pass} values of (3.24 ± 0.95) $x10^{-6}$ $A.cm^{-2}$ for pure Ti and (5 ± 2)$x10^{-8}$ $A.cm^{-2}$ for comparable MAO coatings not functionalized with (bio)molecules [21].

Table 1
Open circuit potential (E_{OCP}), corrosion potential ($E_{(i\ =\ 0)}$), and passivation current density (i_{pass}) values for all specimens.

Specimens	E_{OCP} ($V_{Ag/AgCl}$)	$E_{(i\ =\ 0)}$ ($V_{Ag/AgCl}$)	i_{pass} ($x10^{-8}$ $A.cm^{-2}$)
MAO-control	0.29 ± 0.00	0.14 ± 0.01	2.18 ± 0.69
MAO-PEG	0.28 ± 0.01	0.12 ± 0.02	1.28 ± 0.33
MAO-PEG-AMP	0.19 ± 0.12	0.08 ± 0.07	1.73 ± 0.78

A passivation plateau was observed for all the surfaces (Fig. 7b), followed by a slight increase of the current that may correspond to the degradation of the MAO film, likely caused by the dissolution of calcium and phosphorus [21,37]. This passive domain is clearly increased by treating the MAO coatings with the (bio)molecules, being registered from 0.72 to 0.84 $V_{Ag/AgCl}$ for MAO-control, whereas for MAO-PEG and MAO-PEG-AMP it was observed from 0.77 to 0.94 $V_{Ag/AgCl}$ and 0.81 to 1.00 $V_{Ag/AgCl}$, respectively. This increased extension of the passivation plateau may be related to the oxidation of the immobilized molecules. Ulbricht et al [38] discussed that water content, pH, temperature, exposure to ultraviolet light, presence of enzymes, oxygen or oxidants, strongly affect the stability of polymeric materials. Specifically, compounds like PEG (or surface-bound PEG) and other organic substances (including proteins and peptides) can undergo oxidative degradation [38].

To date, biomolecular coatings are usually focused on their biological implications, and the effect of (bio)molecules on corrosion resistance is poorly investigated. Zhao et al [39] first deposited an MgF_2 layer on a Mg-Zn-Y-Nd alloy and then applied a polydopamine (PDA) coating, which served to further immobilize natural polysaccharides (fucoidan) and bioactive CAG (Cys-Ala-Gly) peptides (derived from type IV collagen) for use in vascular stent applications. The MgF_2 + PDA combination exhibited the highest corrosion resistance in Hanks' solution, presenting the lowest corrosion current density, i_{corr}, of 3.37×10^{-8} $A.cm^{-2}$. Although increasing CAG peptide grafting densities led to higher i_{corr} values (4.41×10^{-7}, 6.96×10^{-7}, and 4.65×10^{-7} $A.cm^{-2}$), the modified surfaces still ensured effective corrosion protection compared

to the uncoated magnesium alloy (1.98×10^{-6} A.cm^{-2}). Nonetheless, to the best of the authors' knowledge, no electrochemical studies have yet examined MAO-treated Ti surfaces that are further functionalized through AMP immobilization. It highlights a notable gap in the existing literature on how such biomolecular layers affect the corrosion behavior of Ti-based systems.

To obtain a comprehensive understanding of the corrosion behavior of each coating, EIS was employed. Representative Nyquist and Bode diagrams, with experimental and fitted data, are presented in Fig. 8. According to the Nyquist diagram (Fig. 8a), all groups presented two semi-circle patterns: a first well distinguished semi-circle, followed by a consistent rising semi-circle pattern, which may suggest that the PEG or PEG-AMP introduction did not modify the corrosion mechanism. However, MAO-PEG and MAO-PEG-AMP coatings have exhibited an increase on the diameter of the first distinct semi-circle (high-middle frequency range), which might be related with the immobilization of the molecules, corresponding to the response of the outmost porous layer of the coating.

Based on the Bode diagrams (Fig. 8b), the coatings showed three-time constants: one corresponding to high frequencies, where the phase angle approached to −70°, −60°, and −50° for MAO-PEG-AMP, MAO-PEG, and MAO-control, respectively. This may be an effect of different exponent n_{ox} of the CPE, probably dependent on the (bio) molecules at the surface. The other two constants correspond to middle-low frequencies; no significant difference was observed on the phase angle for the 10^{-1} to 10 Hz range, with values near −60°. The introduction of PEG and PEG-AMP resulted in a slight increment on the total impedance (|Z|), indicating better corrosion resistance as compared to MAO-control.

The schematic representation of the electrical equivalent circuit (EEC) used for fitting EIS results of the coatings is shown in Fig. 9. A triplex structure is considered, consisting of a barrier film (thin compact oxide layer) at the coating/substrate interface, followed by two thicker porous layers [21,37]. The inner porous layer is characterized by small pores, and the outer porous layer mainly contains larger pores; these bigger cavities may also reach some deeper regions of the coating but not affecting the barrier film. The pair of a resistor R_{bf} and a constant phase element Q_{bf} was associated with the barrier film. Regarding the anodic porous layers, Q_{wall} and $Q_{1/2wall}$ were used as constant phase elements (CPEs) to represent the intact porous wall (outer porous layer) and the porous wall under the outer pores (inner porous layer), respectively. Specifically, no resistor is considered in parallel with these CPEs, due to the high thickness of the corresponding porous layers, leading to extremely elevated resistance values. Other three resistors were included in the EEC, corresponding to the overall electrolyte resistance R_e, as well as the additional resistances of electrolyte filling the outer pores ($R_{e\text{-op}}$) and inner pores ($R_{e\text{-ip}}$).

The immobilization of PEG or PEG-AMP did not modify this general cross-section structure of the MAO coating, and the same EEC was used for MAO-control, MAO-PEG, and MAO-PEG-AMP groups. However, some considerations should be addressed. The immobilization of PEG molecules was dependent on the linkage with surface hydroxyl groups, which were created by O_2 plasma to play as anchors. As the gas plasma may not reach so easily deeper cavities of the MAO coating during the fast activation treatment, it is hypothesized that PEG molecules are more concentrated in top regions of the coating. On the other hand, AMP immobilization was not dependent on specific anchor groups present on the MAO surface, which may facilitate peptide adsorption to the different porous layers during immersion treatment. This distribution of PEG and AMP along the MAO layers was proposed in Fig. 9.

The larger difference between the specimens treated or not with the (bio)molecules was noticed for capacitance and n values corresponding to the outer porous layers, as shown in Table 2 (dataset obtained from the representative EIS spectra for each coating). The average values accompanied by the respective standard deviations were reported in Table S2, Supplementary Material. The impedance of a CPE is defined by Eq. (2) [37,40], where Y_0 is the CPE admittance, $j = \sqrt{-1}$ is the imaginary number, ω is the angular frequency, and n is the dimensionless exponential factor ($-1 \leq n \leq 1$). The n values are influenced by morphology, roughness, and irregularities of surface. For $n = 1$, $n = 0$, or $n = -1$, the CPE behaves as a capacitor, a resistor or an inductor, respectively. All the coatings presented n values higher than 0.75, describing a non-ideal capacitor ($n \approx 1$). Regarding the outer porous layers, the n_{wall} values were higher for MAO-PEG and MAO-PEG-AMP specimens as compared to MAO-control (statistical comparison is presented in Fig. S2, Supplementary Material), which may indicate that the presence of the (bio)molecules makes the surface more uniform (less surface heterogeneity).

$$Z_{CPE} = [Y_0(j\omega)^n]^{-1} \tag{2}$$

The conversion of Q values (see Table S2 in Supplementary Material) into C (capacitance) was performed. The Eq. (3), Eq. (4) and Eq. (5) were derived from Brug's equation [41] and used to calculate C_{wall}, $C_{1/2wall}$ and C_{bf}, respectively:

$$C_{wall} = \left[Q_{wall}\, R_e^{(1-n)}\right]^{1/n} \tag{3}$$

$$C_{1/2wall} = \left[Q_{1/2wall}\, \left(R_e + R_{e-op}\right)^{(1-n)}\right]^{1/n} \tag{4}$$

$$C_{bf} = \left[Q_{bf}\left(\left(\frac{1}{R_e + R_{e-ip}}\right) + \left(\frac{1}{R_{bf}}\right)\right)^{(n-1)}\right]^{1/n} \tag{5}$$

It was verified that the C_{wall} values were lower for MAO-PEG and, mainly, MAO-PEG-AMP coatings comparing with MAO-control (statistical comparison is presented in Fig. S2, Supplementary Material), demonstrating the improvement in the corrosion behavior of the outer

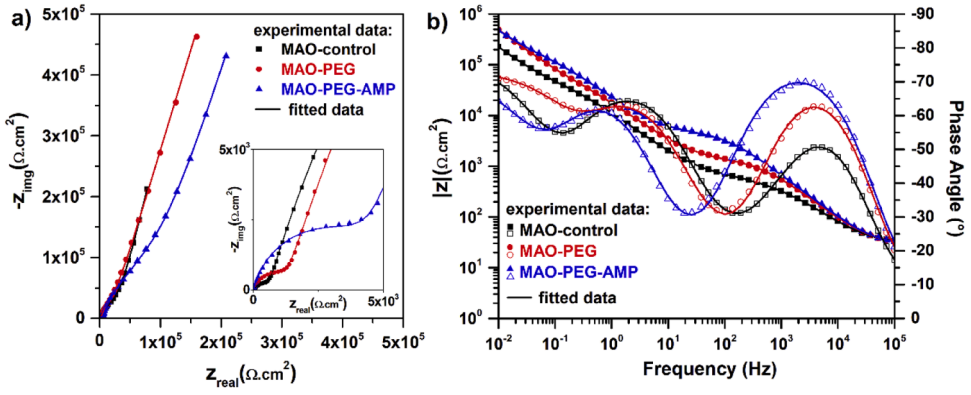

Fig. 8. Representative EIS spectra displayed as (a) Nyquist and (b) Bode diagrams for MAO-control, MAO-PEG and MAO-PEG-AMP coatings immersed in PBS at body temperature.

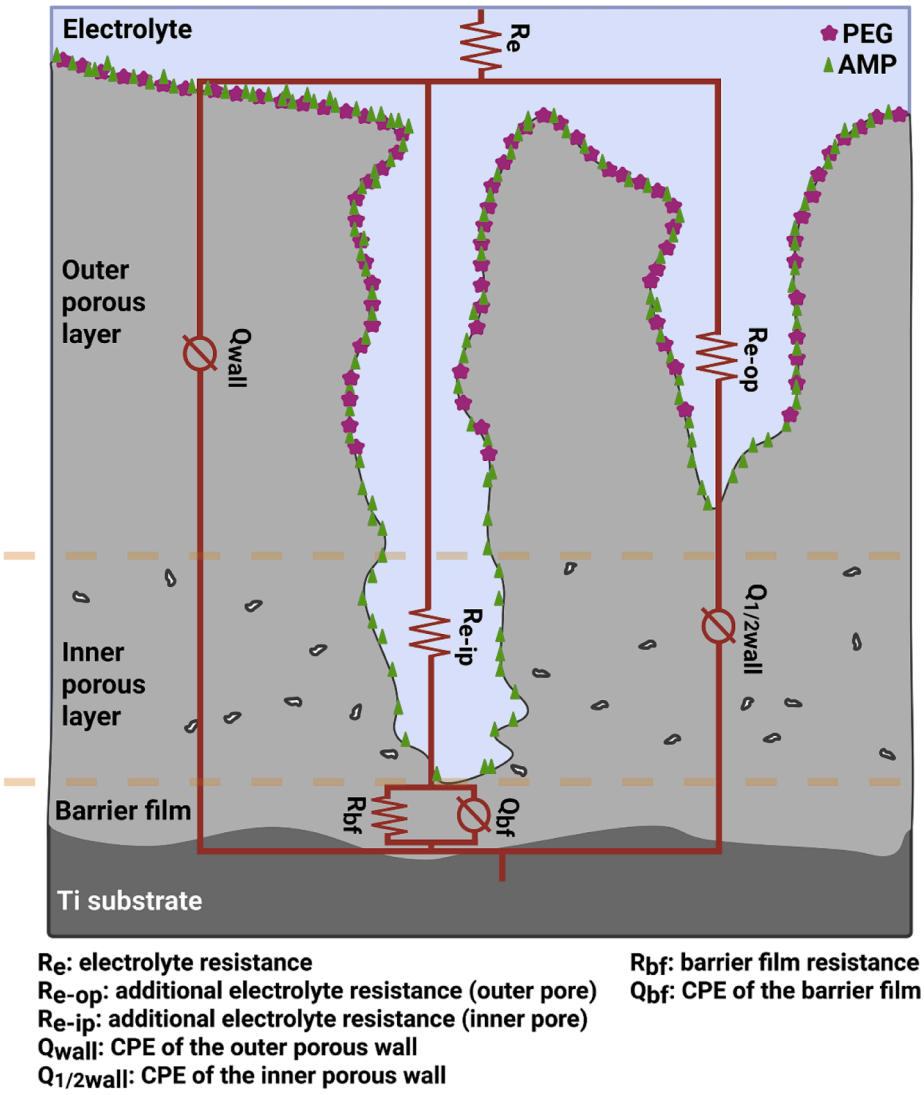

Fig. 9. Schematic representation of EEC used for fitting EIS results of the coatings. Adapted from [37].

Table 2
EEC parameters obtained from EIS spectra for all specimens.

Specimens	C_{bf} ($x10^{-6}$ F. cm^{-2})	n_{bf}	$C_{1/2wall}$ ($x10^{-6}$ F. cm^{-2})	$n_{1/2wall}$	C_{wall} ($x10^{-7}$ F. cm^{-2})	n_{wall}
MAO-control	1.91	0.80	3.87	0.84	1.89	0.79
MAO-PEG	2.30	0.82	3.73	0.83	1.42	0.86
MAO-PEG-AMP	2.05	0.80	3.66	0.80	1.16	0.86

porous layers by the introduction of PEG-AMP. There is no difference for the other parameters corresponding to the inner porous layer and barrier film, which reinforces the influence of the (bio)molecules only on the top regions.

Parfenov et al [42] have attached RGD tripeptide derivatives to MAO TiO_2 coatings with a bisphosphonate linker. However, in their electrochemical tests, the corrosion resistance was deteriorated after the introduction of organic molecules, increasing i_{corr} from (9.45 ± 0.80) x 10^{-9} to (2.16 ± 1.12) x 10^{-7} A.cm^{-2} in Ringer's solution. Using EIS, the authors have stated that the corrosion mechanisms were altered with the presence of the peptide RGD, proposing two different EECs. Without the peptide, the EEC presented *Re* (electrolyte's solution), a porous oxide layer (consisting in a CPE with a resistance R in parallel) and a Warburg diffusion element (Wo) to account for diffusion processes occurring inside the pores in the coating. After peptide attachment, the authors suggested a modification exclusively assigned to the barrier layer, where the charge transfer mechanisms were influenced, by transforming the diffusion-controlled process (described by Wo) into a kinetically controlled process (described by a pair CPE2-R3 in parallel). Nevertheless, the validity of their EECs may be questionable. Diffusion control is not very much expected in MAO-treated Ti (rate of metal oxidation, for example, is expected to be very low) [37]. It also included an outer porous layer resistance, but with a quite low value for this parameter considering the large thickness of this layer; in contrast, the thin passive oxide film from Ti bulk material presented a resistance greater by two orders of magnitude. Moreover, the confirmed presence of peptide RGD at the top MAO layers seems to be disregarded on the corrosion evaluation.

3.3. Corrosion mechanisms

The corrosion mechanism of the MAO coating before and after post-treatment with PEG-AMP is proposed in Fig. 10. Electrochemical results indicate that MAO-control specimens exhibit the same corrosion mechanism as MAO-PEG and MAO-PEG-AMP, with a slight improvement in corrosion resistance following (bio)molecule immobilization. According to previous work employing the same MAO processing

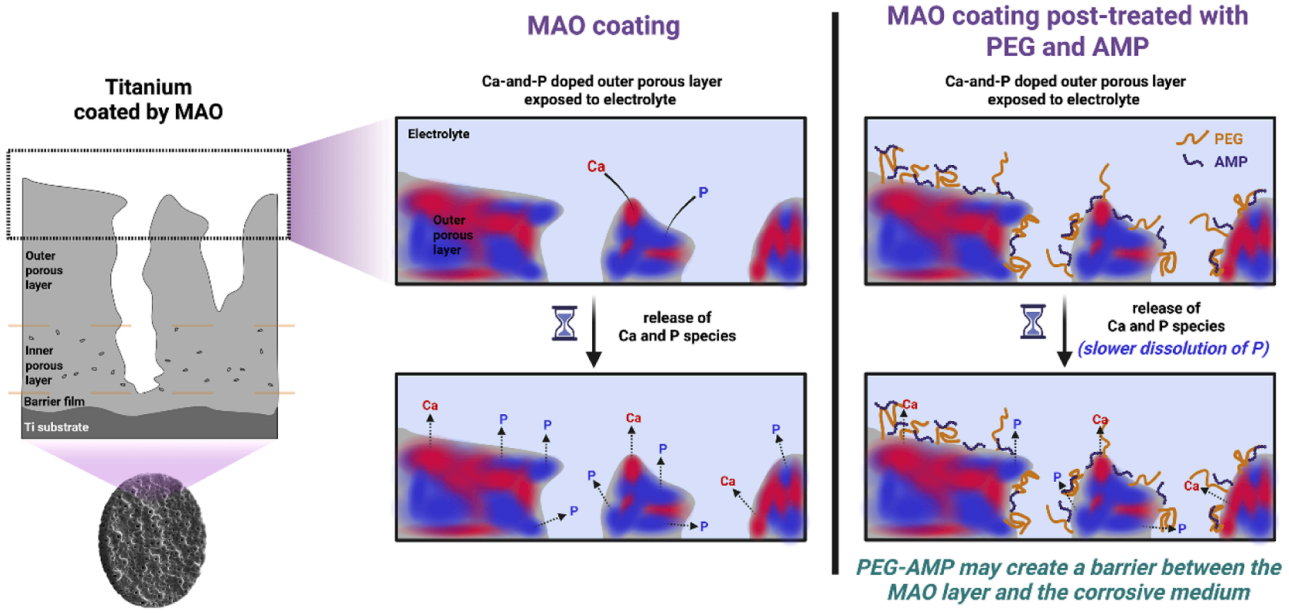

Fig. 10. Suggested corrosion mechanism for MAO coatings (not treated or post-treated with PEG and AMP).

parameters [20], we found that the anodic coating presented a gradient of Ca and P, with both elements being more concentrated in the outer zones of the MAO layer. Moreover, the top surface consisted of calcium carbonate and calcium phosphates. When exposed to a corrosive electrolyte (PBS was applied to simulate the pH, osmolarity, and ion concentration of human body fluids), these Ca and P species gradually leached into the solution over time. Post-treatment with PEG or PEG-AMP may create a barrier between the MAO layer and the corrosive medium, attenuating the dissolution kinetics of the bioactive species, namely the major release of phosphorus observed in Fig. 6a. In particular, MSI-78 is a cationic peptide, with positively charged residues distributed along its chain via lysine (K) amino acids (see Fig. 1). This positive charge may attract phosphate ions (PO_4^{3-}) migrating outward from the outer porous layer and help minimize their leakage into the corrosive electrolyte. From a biomedical perspective, the sustained regulation of phosphorus release may exert a beneficial modulatory effect on host cell responses.

Conversely, calcium can be released as Ca^{2+} species, and the presence of cationic AMP may promote their leakage into the electrolyte through repulsive forces. However, this potential effect was not clearly observed, likely due to the relatively low dissolution of calcium compared with that of phosphorus (Fig. 6b).

3.4. Tribocorrosion behavior

The evolution of OCP before, during, and after sliding together with the COF are depicted in Fig. 11. All the conditions presented stable OCP throughout the tribocorrosion experiment, suggesting that the anodic

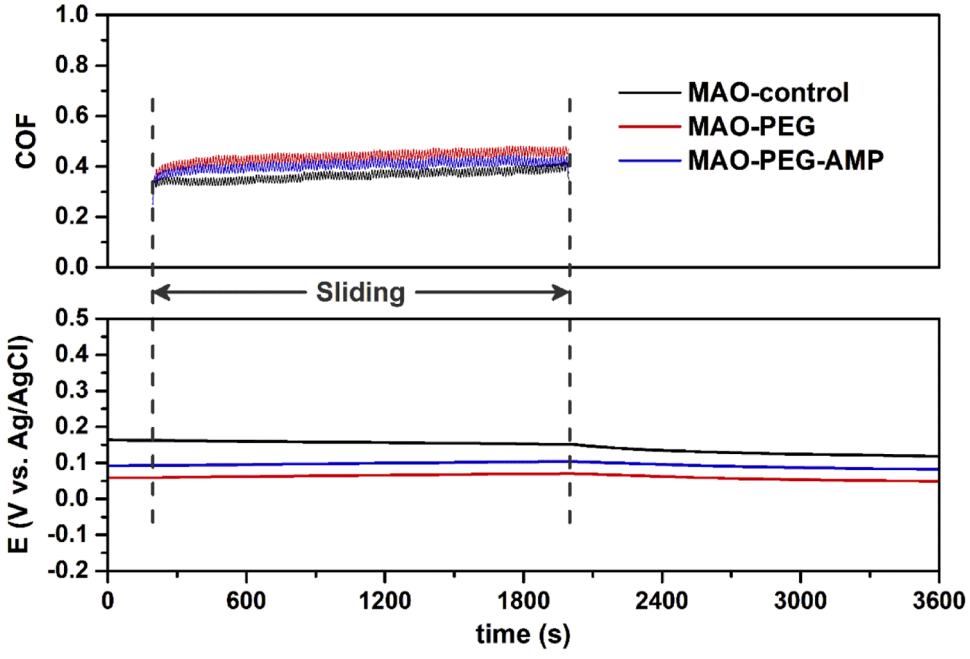

Fig. 11. Evolution of OCP and COF for MAO-control, MAO-PEG and MAO-PEG-AMP specimens during tribocorrosion tests.

coating kept the protection of Ti bulk material. COF values were slightly higher for the (bio)molecule-treated MAO coatings, reaching the highest average values for MAO-PEG surfaces (0.44) and decreasing after AMP adsorption (0.40), in contrast with MAO-control (0.36). However, no abrupt fluctuations in COF profiles were observed during mechanical solicitations. As reported in earlier studies [24,43], similar MAO Ti coatings (without (bio)molecular functionalization) achieved higher COF values (~0.6–0.7) when evaluated using the same alumina counter body, even though the applied normal load was reduced by half (0.50 N) in a 0.9 % NaCl medium.

Polymer-based materials have been used as lubricants through different designs [44], including polymer brushes due to their unique interface behavior. These polymer structures are molecular chains grafted onto a surface, where one end is fixed, and the other end extends outward as a brush-like configuration [44,45]. The conformation of these polymer chains may be changed in response to the electrolyte pH, as well as the concentration and type of ions of the electrolyte in contact. Consequently, alterations in chain conformation can affect hydration levels and then modulate the interfacial friction. Wei et al [46] have proposed lubricating mechanisms for these structures: polymer brushes in a stretched state (usually perpendicular to the grafted surface) could improve the combination with water molecules, thereby showing superior lubrication; on the other side, a more collapsed conformation of the polymer chains can increase the friction between the sliding interfaces. A similar behavior was verified for other polymer brushes-grafted systems [47,48], even tuning lubricating properties from ultra-high friction (COF ~ 1) to super lubrication (COF ~ 10^{-3}). In this work, considering that there were no relevant differences in terms of morphology between the specimen conditions, it is reasonable to assume that the increase in COF values was assigned to the conformation of large and bulky PEG chains grafted onto the MAO surface. These surface polymer chains may be in a more collapsed and entangled state, inducing different tribological contact and a subsequent increase in friction. Further analysis of molecule conformation (through FTIR and/or Raman spectroscopies, small-angle X-ray scattering) is needed to better understand the PEG grafting state, which may be dependent on the type of target substrate, size of molecule chain, and/or type of surrounding electrolyte.

On the other hand, the AMP adsorption onto the PEGylated MAO surfaces (MAO-PEG-AMP coatings) has slightly reduced COF values, acting as lubricating complexes. Trino et al [7] observed a lower friction for TiO_2 rutile surfaces treated with peptide DMP1, implying some lubricating nature of the peptides, which may improve shear-stress distribution. The authors also suggested that the combination of peptides with other organic molecules (such as spacers) at the surface may result in distinct friction behavior, and thereby each surface functionalization condition (peptide/spacer pairs) needs to be investigated individually.

The wear scars of the coatings were observed by SEM in Fig. 12, together with chemical investigation by EDS. Regardless of the (bio) molecule immobilization, only two different zones were found on the wear tracks: unaffected areas, represented by the zones Z1, Z2 and Z5, where the porous structure seems to be preserved and composed of Ca and P originated by the anodic treatment; the other areas (zones Z2, Z4 and Z6) are characterized by pores filled with wear debris (see Fig. S3 in Supplementary Material), eventually forming a compacted MAO layer, where Ca and P are still present, but also mixed with some components from the electrolyte, such as Na, Cl, and K (peaks of phosphorus were also increased, probably due to the presence of phosphates in PBS).

Taking into account the microstructural, structural, and tribo-electrochemical analysis, all the surfaces seem to present the same general tribocorrosion mechanisms, which resembled features previously reported in the literature [23,24,43,49]. As the counter-body slides on the surface, the most protruded zones of the MAO layer are prone to local mechanical damages, due to higher contact pressures with the counter-body. The wear debris released from this partial destruction can be compacted by the counter-body movement, covering the underlying porous structures and eventually forming smooth zones on the

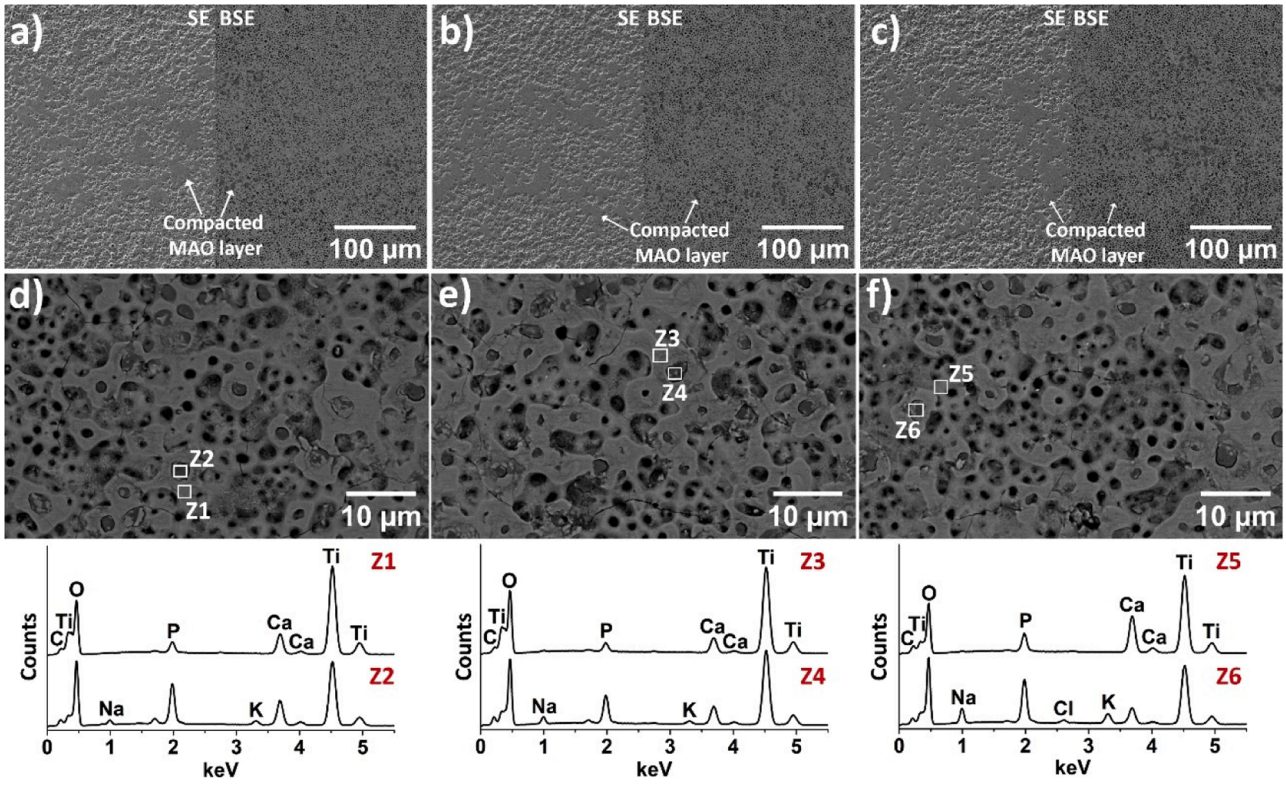

Fig. 12. SEM images of the worn surfaces a),d) MAO-control, b),e) MAO-PEG, and c),f) MAO-PEG-AMP after tribocorrosion tests, together with EDS spectra taken from selected zones.

surface. In this contribution, the MAO layers seem to appropriately withstand the loading forces, not allowing exposure of the substrate likely by the mixture of crystalline TiO_2 phases in the coating (Fig. 5), namely anatase and rutile [22,24,43]. Extreme conditions of loading were purposely applied (contact pressure of 410 MPa) to simulate the worst scenarios and get better understanding of wear mechanisms, being significantly higher than the ones reported for some permanent implants, such as hip (3–9 MPa) [50] and knee (2–32 MPa) [51].

The normal load applied in this study (1 N), although higher than that used in previous investigations [24,43,52], did not allow for a quantitative determination of the wear rate. Mechanical degradation of the MAO layers manifested as a mild polishing of the elevated regions characteristic of the volcano-like surface morphology (Fig. 12 and Fig. S3 in Supplementary Material). As a result, no well-defined wear track could be identified or measured. Extending the test duration or increasing the normal load may facilitate the formation of a measurable wear track, thus enabling robust wear-rate determinations and providing deeper insight into the tribocorrosion behavior of the coatings.

The tribocorrosion performance can be further enhanced through advanced MAO Ti surfaces, achieved by incorporating additives or solid particles into the base electrolyte during the MAO process [53,54]. Such modifications can alter the coating characteristics, leading to increased thickness, reduced porosity (and thus greater compactness), improved hardness, and even imparting a lubricating effect. Nevertheless, the surface immobilization of (bio)molecules onto these specific MAO coatings has yet to be investigated.

In summary, beyond cytocompatibility and antibacterial activity previously identified [28], the sustained tribocorrosion performance observed after PEG-AMP immobilization underscores the potential of multifunctional surfaces. This outcome addresses a critical gap in the current literature, by integrating mechanical and biological aspects with equal priority to meet the complex requirements of next-generation bone implants.

4. Conclusions

The effect of PEG and PEG-AMP on the corrosion and tribocorrosion behavior of MAO TiO_2 surfaces was studied. The functionalization with PEG and PEG-AMP did not alter the porous morphology and bulk chemical composition (Ca/P ratio) of the MAO coatings. Corrosion mechanisms were not significantly affected, but the corrosion resistance was slightly improved by the immobilization of the (bio)molecules, as evidenced by the capacitance values of the outer porous layer (C_{wall}). COF was slightly increased after functionalization with PEG and PEG-AMP; however, all the coatings presented good tribocorrosion behavior, protecting the Ti bulk material, as no variation on OCP was observed during mechanical sliding, as well as there is no evidence of metallic substrate exposure in the wear tracks.

CRediT authorship contribution statement

Natália A. Costa: Writing – original draft, Visualization, Validation, Methodology, Investigation, Formal analysis, Conceptualization. **Alexandra C. Alves:** Writing – review & editing, Validation, Methodology, Investigation, Formal analysis. **André L. Rossi:** Writing – review & editing, Resources, Methodology, Investigation. **Ana R. Ribeiro:** Writing – review & editing, Resources, Methodology. **Cláudia Monteiro:** Writing – review & editing, Methodology, Conceptualization. **M. Cristina L. Martins:** Writing – review & editing, Validation, Supervision, Project administration, Methodology, Funding acquisition, Conceptualization. **Paulo N. Lisboa-Filho:** Writing – review & editing, Validation, Supervision, Project administration, Methodology, Funding acquisition, Conceptualization.

Declaration of competing interest

The authors declare that they have no known competing financial interests or personal relationships that could have appeared to influence the work reported in this paper.

Acknowledgements

This study was financed in part by the Coordenação de Aperfeiçoamento de Pessoal de Nível Superior - Brazil (CAPES) - Finance Codes 88887.600413/2021-00 and 88887.802752/2023-00, and São Paulo Research Foundation (FAPESP) (grants #2020/10125-9 and #2021/11461-5). The authors acknowledge Estrela Neto from Neuro & Skeletal Circuits group (i3S) for the help and availability of the plasma cleaner equipment. The authors acknowledge the following support: (iii) Histology and Electron Microscopy Platform (i3S) for SEM/EDS investigation. The authors would also like to thank the LABNANO/CBPF, where cross-section preparation by FIB and following TEM analysis were performed. This work was carried out in part through the use of the INL Facilities (XRD and XPS analysis) and funded by the European Union's H2020 project Sinfonia (N.857253). Fig. 1 (license n. WP299AY1LJ), Fig. 9 (license n. RB28BOVA7Y), and Fig. 10 (license n. QN298×6Z8O) were created with BioRender.com.

Supplementary materials

Supplementary material associated with this article can be found, in the online version, at doi:10.1016/j.apsadv.2026.100976.

Data availability

Data will be made available on request.

References

[1] S. Spriano, S. Yamaguchi, F. Baino, S. Ferraris, A critical review of multifunctional titanium surfaces: new frontiers for improving osseointegration and host response, avoiding bacteria contamination, Acta Biomater. 79 (2018) 1–22, https://doi.org/10.1016/j.actbio.2018.08.013.
[2] X. Chen, J. Zhou, Y. Qian, L.Z. Zhao, Antibacterial coatings on orthopedic implants, Mater. Today Bio. 19 (2023) 100586, https://doi.org/10.1016/j.mtbio.2023.100586.
[3] H. Chouirfa, H. Bouloussa, V. Migonney, C. Falentin-Daudré, Review of titanium surface modification techniques and coatings for antibacterial applications, Acta Biomater. 83 (2019) 37–54, https://doi.org/10.1016/j.actbio.2018.10.036.
[4] P.M. Alves, C.C. Barrias, P. Gomes, M.C.L. Martins, How can biomaterial-conjugated antimicrobial peptides fight bacteria and be protected from degradation? Acta Biomater. 181 (2024) 98–116, https://doi.org/10.1016/j.actbio.2024.04.043.
[5] J. Buxadera-Palomero, C. Calvo, S. Torrent-Camarero, F.J. Gil, C. Mas-Moruno, C. Canal, D. Rodríguez, Biofunctional polyethylene glycol coatings on titanium: an in vitro-based comparison of functionalization methods, Colloids. Surf. B Biointerfaces. 152 (2017) 367–375, https://doi.org/10.1016/j.colsurfb.2017.01.042.
[6] H. Zhang, P. Zhang, X. Shen, J. Han, H. Wang, H. Qin, B. Wang, J. Qian, A. Udduttula, R. Luo, K. Zhao, Y. Wang, Y. Chen, A cross-linked coating loaded with antimicrobial peptides for corrosion control, early antibacterial, and sequential osteogenic promotion on a magnesium alloy as orthopedic implants, Acta Biomater. 193 (2025) 604–622, https://doi.org/10.1016/j.actbio.2024.12.046.
[7] L.D. Trino, E.S. Bronze-Uhle, A. Ramachandran, P.N. Lisboa-Filho, M.T. Mathew, A. George, Titanium surface bio-functionalization using osteogenic peptides: surface chemistry, biocompatibility, corrosion and tribocorrosion aspects, J. Mech. Behav. Biomed. Mater. 81 (2018) 26–38, https://doi.org/10.1016/j.jmbbm.2018.02.024.
[8] W. Shi, Y. Li, X. Li, M. Ma, G. Shi, J. Yuan, Z. Sun, K. Zhang, C. Jin, W. Liu, Fabrication and long-term in vitro corrosion behavior of MAO coating on biodegradable Mg-3Zn-0.7Mn-0.5Sr alloy, Mater. Today Commun. 47 (2025) 113220, https://doi.org/10.1016/j.mtcomm.2025.113220.
[9] Y. Luo, D. Yu, D. Liu, S. Li, J. Wu, L. Huang, X. Xu, Y. Hua, Effects of current density on microstructure and tribological property of micro-arc oxidation coating on B4C reinforced Al-Zn-Mg-Cu-Zr aluminum matrix composite, Mater. Des. 261 (2026) 115404, https://doi.org/10.1016/j.matdes.2025.115404.
[10] M. Deng, P. Zhang, Z. Kang, Y. Mao, Q. Xiong, W. Zhang, Z. Cai, L. Gu, Comparative study on the fretting and sliding wear properties of micro-arc

oxidation-treated aluminum alloy at different temperatures, Tribol. Int. 198 (2024) 109847, https://doi.org/10.1016/j.triboint.2024.109847.
[11] Y. Hao, Y. Du, L. Wang, Y. Cao, Z. Ye, C. Wang, Tailored micro-arc oxidation coatings to match with parylene for enhanced tribological performance of Ta-12W alloys, Ceram. Int. 50 (2024) 53835–53850, https://doi.org/10.1016/j.ceramint.2024.10.237.
[12] X. Liu, Q. Sui, W. Wang, H. Liu, Biological activity of tantalum oxide coating doped with calcium and strontium by micro-arc oxidation under osteoimmunomodulation, Surf. Interfaces. 50 (2024) 104500, https://doi.org/10.1016/j.surfin.2024.104500.
[13] T.W. Clyne, S.C. Troughton, A review of recent work on discharge characteristics during plasma electrolytic oxidation of various metals, Int. Mater. Rev. 64 (2019) 127–162, https://doi.org/10.1080/09506608.2018.1466492.
[14] M. Aliofkhazraei, D.D. Macdonald, E. Matykina, E.V. Parfenov, V.S. Egorkin, J. A. Curran, S.C. Troughton, S.L. Sinebryukhov, S.V. Gnedenkov, T. Lampke, F. Simchen, H.F. Nabavi, Review of plasma electrolytic oxidation of titanium substrates: mechanism, properties, applications and limitations, Appl. Surf. Sci. Adv. 5 (2021) 100121, https://doi.org/10.1016/j.apsadv.2021.100121.
[15] E. Nikoomanzari, M. Karbasi, W.C.M.A. Melo, H. Moris, K. Babaei, S. Giannakis, A. Fattah-alhosseini, Impressive strides in antibacterial performance amelioration of Ti-based implants via plasma electrolytic oxidation (PEO): a review of the recent advancements, Chem. Eng. J. 441 (2022) 136003, https://doi.org/10.1016/j.cej.2022.136003.
[16] G. Li, F. Ma, P. Liu, S. Qi, W. Li, K. Zhang, X. Chen, Review of micro-arc oxidation of titanium alloys: mechanism, properties and applications, J. Alloys. Compd. 948 (2023) 169773, https://doi.org/10.1016/j.jallcom.2023.169773.
[17] B. Makurat-Kasprolewicz, A. Ossowska, Recent advances in electrochemically surface treated titanium and its alloys for biomedical applications: a review of anodic and plasma electrolytic oxidation methods, Mater. Today Commun. 34 (2023) 105425, https://doi.org/10.1016/j.mtcomm.2023.105425.
[18] S. Sikdar, P.V. Menezes, R. Maccione, T. Jacob, P.L. Menezes, Plasma electrolytic oxidation (PEO) process - processing, properties, and applications, Nanomaterials 11 (2021), https://doi.org/10.3390/nano11061375.
[19] F. Simchen, M. Sieber, A. Kopp, T. Lampke, Introduction to plasma electrolytic oxidation - an overview of the process and applications, Coatings 10 (2020) 628, https://doi.org/10.3390/coatings10070628.
[20] N.A. Costa, A.R. Ribeiro, A.L. Rossi, C. Monteiro, P.N. Lisboa-Filho, M.C.L. Martins, Effect of NaOH etching and oxygen plasma treatments on surface characteristics and their potential to activate micro-arc oxidized TiO2 coatings, Appl. Surf. Sci. 682 (2025) 161748, https://doi.org/10.1016/j.apsusc.2024.161748.
[21] A.C. Alves, A.I. Costa, F. Toptan, J.L. Alves, I. Leonor, E. Ribeiro, R.L. Reis, A.M. P. Pinto, J.C.S. Fernandes, Effect of bio-functional MAO layers on the electrochemical behaviour of highly porous Ti, Surf. Coat. Technol. 386 (2020) 125487, https://doi.org/10.1016/j.surfcoat.2020.125487.
[22] F.G. Oliveira, A.R. Ribeiro, G. Perez, B.S. Archanjo, C.P. Gouvea, J.R. Araújo, A.P. C. Campos, A. Kuznetsov, C.M. Almeida, M.M. Maru, C.A. Achete, P. Ponthiaux, J. P. Celis, L.A. Rocha, Understanding growth mechanisms and tribocorrosion behaviour of porous TiO2 anodic films containing calcium, phosphorous and magnesium, Appl. Surf. Sci. 341 (2015) 1–12, https://doi.org/10.1016/j.apsusc.2015.02.163.
[23] N.A. Costa, A.L. Rossi, A.C. Alves, A.M.P. Pinto, F. Toptan, L.A. Rocha, Growth mechanisms and tribocorrosion behavior of bio-functionalized ZrO2 nanoparticles-containing MAO coatings formed on Ti-40Nb alloy, J. Bio- Tribo-Corros. 7 (2021), https://doi.org/10.1007/s40735-021-00488-6.
[24] A.I. Costa, F. Viana, F. Toptan, Preliminary tribocorrosion evaluation of bio-functionalized Ti doped with Ca-P-Sr, Mater. Lett. 283 (2021) 128775, https://doi.org/10.1016/j.matlet.2020.128775.
[25] I. da S.V. Marques, M.F. Alfaro, N.C. da Cruz, M.F. Mesquita, C. Sukotjo, M. T. Mathew, V.A.R. Barão, S. Vieira, M. Fernanda, N. Cristino, M. Ferraz, C. Takoudis, C. Sukotjo, M.T. Mathew, V. Adelino, R. Bara, Tribocorrosion behavior of biofunctional titanium oxide films produced by micro-arc oxidation: synergism and mechanisms, J. Mech. Behav. Biomed. Mater. 60 (2016) 8–21, https://doi.org/10.1016/j.jmbbm.2015.12.030.
[26] C. Monteiro, M. Fernandes, M. Pinheiro, S. Maia, C.L. Seabra, F. Ferreira-da-silva, F. Costa, S. Reis, P. Gomes, M.C.L. Martins, Antimicrobial properties of membrane-active dodecapeptides derived from MSI-78, Biochim. Biophys. Acta - Biomembr. 1848 (2015) 1139–1146, https://doi.org/10.1016/j.bbamem.2015.02.001.
[27] B. Costa, J. Coelho, V. Silva, H. Shahrour, N.A. Costa, A.R. Ribeiro, S.G. Santos, F. Costa, G. Martínez-de-Tejada, C. Monteiro, M.C.L. Martins, Dhvar5- and MSI78-coated titanium are bactericidal against methicillin-resistant Staphylococcus aureus, immunomodulatory and osteogenic, Acta Biomater. 191 (2025) 98–112, https://doi.org/10.1016/j.actbio.2024.11.016.
[28] N.A. Costa, C. Monteiro, L. Grenho, A.R. Ribeiro, V. Leiro, M.H. Fernandes, P. N. Lisboa-Filho, M.C.L. Martins, Exploring immobilization strategies of antimicrobial peptides onto MAO-treated titanium to fight MRSA colonization and preserve osteogenic activity, Mater. Today Bio 37 (2026) 102896, https://doi.org/10.1016/j.mtbio.2026.102896.
[29] N.A. Costa, D.R.N. Correa, P.N. Lisboa-Filho, T.S.P. Sousa, C.R. Grandini, L. A. Rocha, Influence of the molybdenum on characteristics of oxide films produced by micro-arc oxidation on Ti-15Zr-based alloys, Surf. Coat. Technol. 408 (2021) 126856, https://doi.org/10.1016/j.surfcoat.2021.126856.
[30] M.C. Rossi, F.J.B. Bezerra, R.A. Silva, B.P. Crulhas, C.J.C. Fernandes, A. S. Nascimento, V.A. Pedrosa, P. Padilha, W.F. Zambuzzi, Titanium-released from dental implant enhances pre-osteoblast adhesion by ROS modulating crucial intracellular pathways, J. Biomed. Mater. Res. - A 105 (2017) 2968–2976, https://doi.org/10.1002/jbm.a.36150.
[31] A. Santos, J. Teixeira, C. Fonzar, E. Rangel, N. Cruz, P.N. Lisboa-Filho, A tribological investigation of the titanium oxide and calcium phosphate coating electrochemical deposited on titanium, Metals 13 (2023) 410, https://doi.org/10.3390/met13020410.
[32] A.A. Santos, J.V.U. Teixeira, C.A.F. Pintão, D.R.N. Correa, C.R. Grandini, P. N. Lisboa-Filho, Ti-15Zr and Ti-15Zr-5Mo biomaterials alloys: an analysis of corrosion and tribocorrosion behavior in phosphate-buffered saline solution, Materials 16 (2023) 1826, https://doi.org/10.3390/ma16051826.
[33] S. Fu, K. Zhang, X. Chen, P. Liu, H. Zhou, F. Ma, Effect of Nb content and micro-arc oxidation on the microstructure, corrosion resistance, and biological properties of coatings on TiZrNb alloys, Ceram. Int. 51 (2025) 54572–54581, https://doi.org/10.1016/j.ceramint.2025.09.186.
[34] J. Zhao, L. Liu, F. Ma, P. Liu, S. Qi, W. Li, K. Zhang, X. Chen, The mechanical and biological performance of zinc-containing micro-arc oxidation film on titanium implant, Ceram. Int. 51 (2025) 13090–13099, https://doi.org/10.1016/j.ceramint.2025.01.155.
[35] E. Lokeshkumar, C. Premchand, P. Manojkumar, R. Shishir, L.R. Krishna, K. G. Prashanth, N. Rameshbabu, Effect of electrolyte composition on the surface characteristics of plasma electrolytic oxidation coatings over Ti-40Nb alloy, Surf. Coat. Technol. 465 (2023) 129591, https://doi.org/10.1016/j.surfcoat.2023.129591.
[36] H. Pan, H. Lu, G. Xu, Z. Fan, F. Yang, P. Liu, Preparation of MAO-Ni/ZrO2 composite coating on titanium alloys by micro-arc oxidation and relatively high voltage cathodic deposition techniques, J. Alloys. Compd. 1010 (2025) 178083, https://doi.org/10.1016/j.jallcom.2024.178083.
[37] A.C. Alves, F. Wenger, P. Ponthiaux, J.-P. Celis, A.M. Pinto, L.A. Rocha, J.C. S. Fernandes, Corrosion mechanisms in titanium oxide-based films produced by anodic treatment, Electrochim. Acta 234 (2017) 16–27, https://doi.org/10.1016/j.electacta.2017.03.011.
[38] J. Ulbricht, R. Jordan, R. Luxenhofer, On the biodegradability of polyethylene glycol, polypeptoids and poly(2-oxazoline)s, Biomaterials 35 (2014) 4848–4861, https://doi.org/10.1016/j.biomaterials.2014.02.029.
[39] Y. Zhao, Y. Wang, L. Chen, L. Bai, S. Guan, Co-immobilization of natural marine polysaccharides and bioactive peptides on ZE21B magnesium alloy to enhance hemocompatibility and cytocompatibility, Int. J. Biol. Macromol. 272 (2024) 132747, https://doi.org/10.1016/j.ijbiomac.2024.132747.
[40] A.R. Lima, A.M.P. Pinto, F. Toptan, A.C. Alves, Impact of simulated inflammation and food breakdown on the synergistic interaction between corrosion and wear on titanium, Corros. Sci. 228 (2024) 111839, https://doi.org/10.1016/j.corsci.2024.111839.
[41] M.E. Orazem, B. Tribollet. Electrochemical Impedance Spectroscopy, 2nd ed., Jonh Wiley & Sons, New Jersey, 2017.
[42] E. Parfenov, L. Parfenova, V. Mukaeva, R. Farrakhov, A. Stotskiy, A. Raab, K. Danilko, N. Rameshbabu, R. Valiev, Biofunctionalization of PEO coatings on titanium implants with inorganic and organic substances, Surf. Coat. Technol. 404 (2020) 126486, https://doi.org/10.1016/j.surfcoat.2020.126486.
[43] A.I. Costa, L. Sousa, A.C. Alves, F. Toptan, Tribocorrosion behaviour of bio-functionalized porous Ti surfaces obtained by two-step anodic treatment, Corros. Sci. 166 (2020) 108467, https://doi.org/10.1016/j.corsci.2020.108467.
[44] G. Liu, Y. Feng, N. Zhao, Z. Chen, J. Shi, F. Zhou, Polymer-based lubricating materials for functional hydration lubrication, Chem. Eng. J. 429 (2022) 132324, https://doi.org/10.1016/j.cej.2021.132324.
[45] J. Chen, J. Wang, P. Qi, X. Li, B. Ma, Z. Chen, Q. Li, Y. Zhao, K. Xiong, M.F. Maitz, N. Huang, Biocompatibility studies of poly(ethylene glycol)-modified titanium for cardiovascular devices, J. Bioact. Compat. Polym. 27 (2012) 565–584, https://doi.org/10.1177/0883911512461108.
[46] Q. Wei, M. Cai, F. Zhou, W. Liu, Dramatically tuning friction using responsive polyelectrolyte brushes, Macromolecules 46 (2013) 9368–9379, https://doi.org/10.1021/ma401537j.
[47] J. Yang, H. Chen, S. Xiao, M. Shen, F. Chen, P. Fan, M. Zhong, J. Zheng, Salt-responsive zwitterionic polymer brushes with tunable friction and antifouling properties, Langmuir. 31 (2015) 9125–9133, https://doi.org/10.1021/acs.langmuir.5b02119.
[48] R. Zhang, S. Ma, Q. Wei, Q. Ye, B. Yu, J. Van Der Gucht, F. Zhou, The weak interaction of surfactants with polymer brushes and its impact on lubricating behavior, Macromolecules 48 (2015) 6186–6196, https://doi.org/10.1021/acs.macromol.5b01267.
[49] A.C. Alves, F. Oliveira, F. Wenger, P. Ponthiaux, J.P. Celis, L.A. Rocha, Tribocorrosion behaviour of anodic treated titanium surfaces intended for dental implants, J. Phys. D. Appl. Phys. 46 (2013) 404001, https://doi.org/10.1088/0022-3727/46/40/404001.
[50] H. Yoshida, A. Faust, J. Wilckens, M. Kitagawa, J. Fetto, E.Y.S. Chao, Three-dimensional dynamic hip contact area and pressure distribution during activities of daily living, J. Biomech. 39 (2006) 1996–2004, https://doi.org/10.1016/j.jbiomech.2005.06.026.
[51] A. Sharma, R.D. Komistek, C.S. Ranawat, D.A. Dennis, M.R. Mahfouz, In vivo contact pressures in total knee arthroplasties, J. Arthroplasty. 22 (2007) 404–416, https://doi.org/10.1016/j.arth.2006.07.008.
[52] L. Sousa, N.A. Costa, A. Rossi, S. Simões, F. Toptan, A.C. Alves, Micro-arc and thermal oxidized titanium matrix composites for tribocorrosion-resistant

biomedical implants, Surf. Coat. Technol. 485 (2024) 130854, https://doi.org/10.1016/j.surfcoat.2024.130854.
[53] T. Fang, C. Guo, Y. Li, D. Zhang, H. Sun, Y. Wan, C. Qi, Effect of sodium lignosulfonate as an additive in enhancing the corrosion and tribocorrosion behavior of micro-arc oxidation coatings on titanium alloy, Int. J. Biol. Macromol. 307 (2025) 141960, https://doi.org/10.1016/j.ijbiomac.2025.141960.
[54] E. Ogur, A.C. Alves, F. Toptan, Advancing titanium-based surfaces via micro-arc oxidation with solid substance incorporation: a systematic review, Mater. Today Commun. 41 (2024) 110343, https://doi.org/10.1016/j.mtcomm.2024.110343.